Physical Science International Journal

18(2): 1-11, 2018; Article no.PSIJ.41673
ISSN: 2348-0130

High Plasticity of an Iron Aluminide-based Material at Low Temperatures

V. Šíma[1*], P. Minárik[1], M. Cieslar[1], R. Král[1], P. Málek[1], T. Chráska[2], F. Lukáč[2], H. Seiner[3] and F. Průša[4]

[1]Faculty of Mathematics and Physics, Charles University, Ke Karlovu 5, Praha 2, CZ-12116, Czech Republic.
[2]Institute of Plasma Physics AS CR, Za Slovankou 1782/3, Praha 8, CZ-18200, Czech Republic.
[3]Institute of Thermomechanics AS CR, Dolejškova 5, Praha 8, CZ-18200, Czech Republic.
[4]Department of Metals and Corrosion Engineering, UCT Prague, Technická 5, Praha 6, CZ -16628, Czech Republic.

Authors' contributions

This work was carried out in collaboration between all authors. All authors read and approved the final manuscript.

Article Information

DOI: 10.9734/PSIJ/2018/41673
Editor(s):
(1) Marian Apostol, Professor, Theoretical Physics, Institute for Atomic Physics, Magurele-Bucharest, Romania.
(2) Dr. Christian Brosseau, Distinguished Professor, Department of Physics, Université de Bretagne Occidentale, France.
Reviewers:
(1) Hossam Ahmed Mohamed Halfa, Central Metallurgical Research & Development Institute, Egypt.
(2) Qiang Li, Weifang University of Technology, P.R. China.
Complete Peer review History: http://www.sciencedomain.org/review-history/24893

Original Research Article

Received 17th March 2018
Accepted 21st May 2018
Published 30th May 2018

ABSTRACT

Aims: To compare surprisingly high plasticity in compression at low temperature of high-quality compacts prepared by spark plasma sintering from atomized Fe-30.8Al-0.35Zr-0.11B (at%) powder with tensile tests at the same conditions.
Study Design: Compressive tests and tensile tests at room temperature and at 77 K, scanning and transmission electron microscopy, measurements of Young's and shear moduli data of the sintered material from room temperature to 80 K.
Place and Duration of Study: Faculty of Mathematics and Physics, Institute of Plasma Physics, Institute of Thermomechanics, Department of Metals and Corrosion Engineering, between October 2015 and November 2017.
Methodology: The feedstock powder was prepared using atomization in argon and consolidated by

**Corresponding author: E-mail: sima@met.mff.cuni.cz;*

spark plasma sintering method. The microstructure and phase composition of the sintered samples were characterized by X-ray diffraction (XRD), scanning electron microscopy (SEM) with electron backscatter diffraction (EBSD) and by transmission electron microscopy (TEM). Mechanical properties of the feedstock powder were characterized by microhardness data, the compacts were in addition tested in compression and in tension. The elastic properties (Young's and shear moduli) of the examined material were measured by a combination of two ultrasonic methods: the pulse-echo method and the resonant ultrasound spectroscopy.

Results: High plasticity (plastic strain more than 30% without failure) was observed in compressive tests at room temperature and at 77 K. Electron microscopy observations revealed the dominating role of dislocation motion in compression at low temperatures. The ductility measured at tensile tests, on the other hand, was only about 1% with a typical brittle failure.

Conclusion: The TEM observations confirm that dislocations enable the plastic flow in compression at low temperatures. The poor ductility in tension is not an intrinsic behavior of the alloy, but it results from the nucleation and opening of nano/microcracks between sintered powder particles and/or cavities in partly hollow atomized particles.

Keywords: Intermetallics; powder metallurgy; mechanical properties; scanning electron microscopy; transmission electron microscopy.

1. INTRODUCTION

Iron aluminides based on FeAl and Fe_3Al have been widely studied, mainly because of their excellent high temperature oxidation and corrosion properties. However, poor formability and ductility, particularly at room temperature, present a serious problem for the industrial application of these materials. There are many factors influencing the plasticity of these materials (e.g. testing environment, Al content, substitutional alloying, dispersed particles, grain size, quenched-in vacancies) [1-5].

Spark plasma sintering (SPS) is a rapid powder consolidation technique that uses uniaxial pressure and heat generated by pulsed direct electric current. Powder densification can be achieved at significantly lower temperatures and shorter times by SPS than by conventional sintering thereby limiting grain growth and preserving the fine microstructure in the SPS consolidated samples [6].

The SPS procedure is often used to sinter powder prepared by mechanical alloying of elemental powders or by milling. Both the milling and the mechanical alloying are used to achieve mechanical activation of particle surfaces and grain refinement. In both cases the milled powder is highly reactive with a heavily deformed microstructure. SPS is also used for powders prepared by gas atomization of an alloy under argon. Sintering of such powders usually leads to a bulk material with improved hardness and strength [7].

The previous studies confirmed the advantages of the SPS-method by successful fabrication of dense fine-grained Fe-Al materials with promising mechanical properties [7-10].

In our previous unpublished work, cryo-milling of an atomized powder of an iron aluminide-based alloy was performed in liquid nitrogen at 77 K. The microstructure of powder particles before and after milling was compared. We observed clear signs of high intrinsic plasticity of the milled polycrystalline powder particles and no signs of brittle cracking (see below).

In the present work, we exploit the low temperature plasticity of the feedstock powder to prepare a dense bulk material with similar and unusual mechanical properties at low temperatures. The primary scope of this study is to report and discuss the observed high plasticity of this material at room temperature and at 77 K.

2. MATERIALS AND METHODS

The feedstock powder was prepared using atomization in argon by LERMPS/PERSEE company (France). The size distribution of spherical particles is characterized by d_{10} = 13.7 μm, d_{50} = 29.0 μm, d_{90} = 51.2 μm as determined by laser granulometry. The chemical analysis of Al, B and Zr in the atomized powder was performed by ICP-OES method using the Iris Intrepid HR, Thermo Scientific. Carbon content was determined by absorption spectrometer LECO CS-444. The oxygen analysis was performed using an absorption spectrometer LECO TC-300.

The atomized powder was consolidated using two different devices: SPS 10-4 apparatus (Thermal Technology LLC) and FCT HP D10 apparatus. Graphite foil was used to separate the SPS graphite tools (die and punches) with a diameter of 20 mm (50 mm for FCT apparatus) from the sintered powder. The graphite foil was later replaced by a tungsten foil, which successfully prevented contamination of the sintered sample by carbon. The powder in the die was heated to the sintering temperature of 1373 K (1273 K for FCT) with a heating rate of 200 K/min (100 K/min for FCT). A pressure of 70 MPa (48 MPa for FCT) was applied and maintained until completion of sintering. The dwell time at 1373 K (1273 K for FCT) was 3 min (30 min for FCT), followed by fast cooling (200 K/min) to 1123 K and then by slower cooling (100 K/min) to room temperature. This choice of sintering parameters is close to the SPS conditions used in [10]. The dimensions of the sintered cylindrical samples were Ø 19 mm x 5 mm (Ø 49 mm x 30 mm for FCT).

The microstructure and phase composition of the sintered samples were characterized by X-ray diffraction (XRD), scanning electron microscopy (SEM) with electron backscatter diffraction (EBSD) and by transmission electron microscopy (TEM). XRD measurements were performed using a Bragg Brentano θ/2θ Bruker X-ray diffractometer, type D8 (Cu K_{α} and Co $K_{\alpha 1}$ radiation). SEM observations were performed using Zeiss Auriga Compact Crossbeam® microscope equipped with EDAX EBSD camera DigiView 5. The identification and visualization of grains was made using the EBSD method by orientation imaging maps. TEM specimens were prepared by mechanical grinding and polishing of thin targets to a thickness of about 100 μm, and thinning to electron transparency using a Struers Tenupol 2 twin jet electrolytic polisher. TEM observations were performed using a JEOL 2000FX electron microscope.

Mechanical properties of the feedstock powder were characterized using a Qness Q10A microhardness tester with Vickers load of 25 gram. The same measurements were made on sintered samples in different parts of cylindrical SPS discs, parallel and perpendicular to the cylindrical axis. Cuboid-shaped compressive samples, typically of 4.9 x 3.5 x 3.5 mm^3, were sectioned by diamond saw from the SPS disk parallel and perpendicular to the axis of the disk. Samples for tensile tests with round cross-section (Ø4 mm) and threaded shoulders were cut parallel to the axis of the bigger SPS-disk. The tests were performed in air at RT and in liquid nitrogen at 77 K with an initial strain rate of 1.0 x 10^{-3} s^{-1}, using an Instron 1186 universal testing machine.

The elastic properties (Young's and shear moduli) of the examined material were measured by a combination of two ultrasonic methods: the pulse-echo method [11] and the resonant ultrasound spectroscopy [12,13]. For the ultrasonic measurements, a perfect cuboid sample of dimensions approximately 2.0 x 3.0 x 4.5 mm^3 was used. Firstly, the velocities of longitudinal and shear ultrasonic waves in three directions perpendicular to the faces of the sample were measured at RT (295 K) using the pulse-echo (P-E) method in order to confirm the assumed elastic isotropy of the compact. The outputs of the P-E method also enabled direct calculation of the Young's modulus *E* and the shear modulus *G*. These values were then used as initial approximations for the inverse procedure in the resonant ultrasound spectroscopy (RUS) method. Secondly, the RUS method was applied to determine accurately the elastic constants in the temperature range from RT to 80 K.

3. RESULTS AND DISCUSSION

3.1 Material Characterization

The results of the chemical analysis of the atomized powder are displayed in Table 1.

The XRD pattern (the red curve in Fig. 1) of the as-received atomized powder showed the presence of the ordered B2 phase[1]. The Rietveld profile analysis of the XRD powder pattern revealed about 0.6 wt.% of the λ_1 hexagonal C14 Laves phase in the atomized powder, in agreement with former observations [14,15].

The microstructure of individual atomized powder particles was successfully determined by SEM and EBSD methods (Fig. 2). Some of the particles have a spherical cavity inside (Fig. 2 below). These particles solidified with inside argon bubbles during atomization process.

The microstructure of atomized powder particles, which were mechanically activated by milling at

[1] The fully developed $D0_3$ equilibrium structure with fcc Bravais lattice and doubled lattice parameter (a = 0.57914(2) nm) was observed after annealing of the powder for 408 h at 693 K under an argon atmosphere.

77 K, is dramatically changed and shows clear signs of the intrinsic low temperature plasticity (i.e. compressive and shear plastic strain) (Fig. 3). The milled powder grains possess heavily strained and disordered A2 (bcc) crystal structure. The A2 crystal structure of the cryomilled powder and the absence of the B2 long-range ordered phase were confirmed also by XRD measurement.

Table 1. Chemical composition of the atomized powder (± standard deviation)

Element	Fe	Al	B	C	O	Zr
at.%	bal.	30.8 ± 0.2	0.109 ± 0.005	0.059 ± 0.001	0.132 ±0.003	0.355 ± 0.005

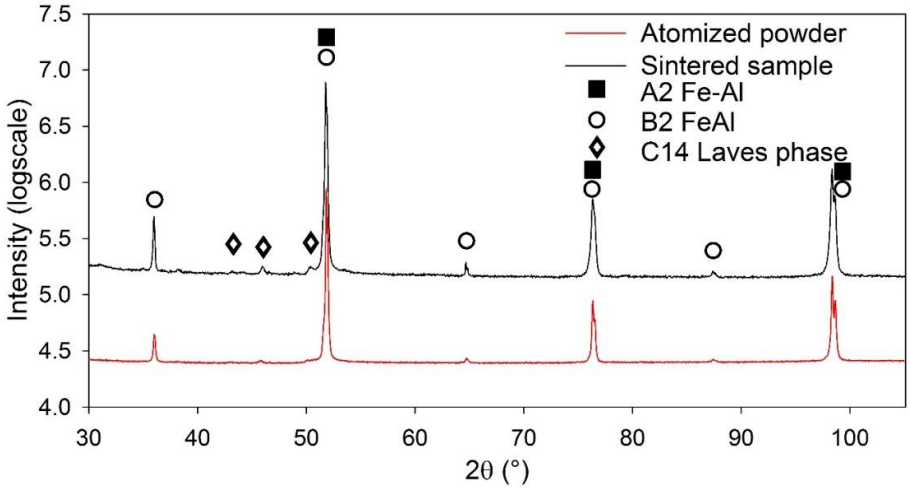

Fig. 1. XRD patterns of the atomized powder and sintered sample

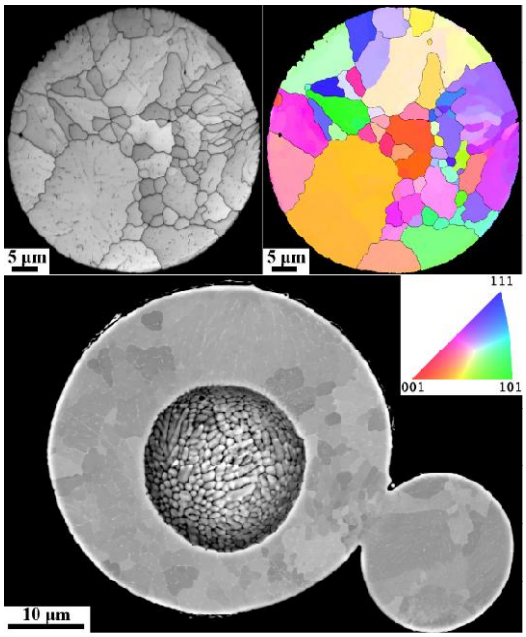

Fig. 2. The microstructure of an atomized powder particle observed by EBSD method (image quality map and orientation imaging map – upper images) and a particle with spherical cavity (SEM channeling contrast - bottom)

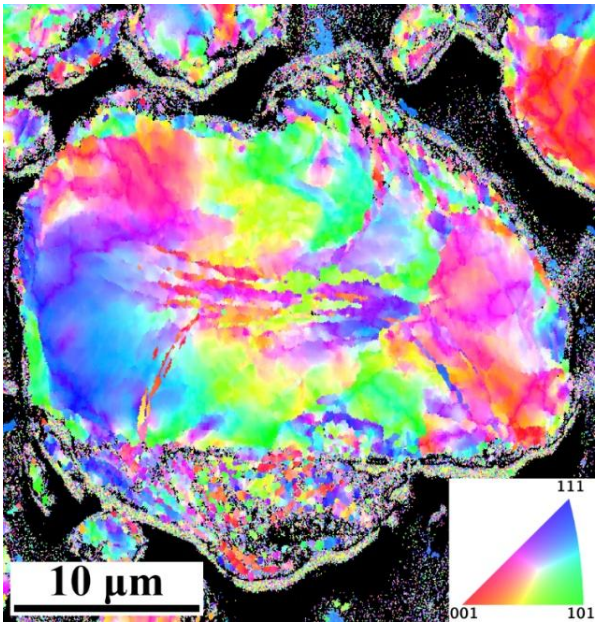

Fig. 3. Orientation imaging map of a cryo-milled (77 K) powder particle with the disordered A2 (bcc) structure

Inspection of all sintered samples by electron microscopy revealed fully dense microstructure without any noticeable porosity. The sintered microstructure resembles the microstructure of atomized particles with very similar grains of the ordered B2 structure (Fig. 4).

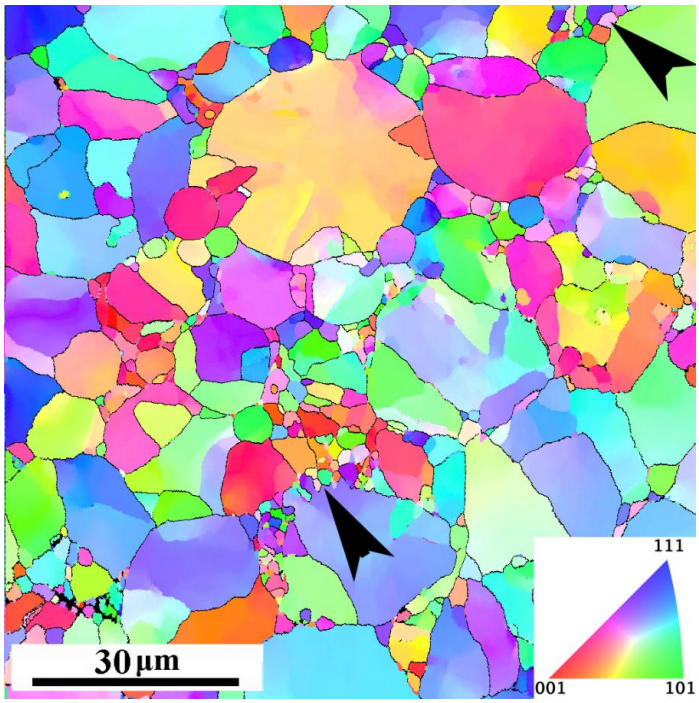

Fig. 4. Orientation imaging map of the sintered bulk material with the ordered B2 structure. The arrows point to regions with fine grains

The sintered microstructure contains also regions with new fine grains (Fig. 4) filling up the volume among original powder particles. The fine grains must have grown during the sintering process. The resulting microstructure has therefore a bimodal or multimodal distribution of grain sizes. XRD pattern of the sintered material (see Fig. 1) showed again the presence of the ordered B2 phase with small amount of the λ_1 hexagonal C14 Laves phase.

Note that surface of several sintered samples was in contact with the graphite foil during the SPS process. It resulted in the formation of κ-$Fe_3AlC_{0.5}$ carbide particles extending several micrometers deep into the sintered material. Substitution of the graphite foil by the tungsten foil fully prevented the formation of the carbide.

3.2 Deformation Behavior

Mechanical properties were studied using microhardness measurements at room temperature (RT) and using both compression and tensile tests at RT and 77 K.

The results of all microhardness measurements are summarized in Table 2. As can be seen from measured hardness values of SPS samples and their standard deviations, the bulk material is homogeneous in the entire volume and the sintering process did not lead to a measurable deviation from microhardness values of the feedstock powder particles.

True stress vs logarithmic plastic strain curves are shown in Fig. 5, the yield strength, maximum strength and logarithmic plastic strain values with their standard deviations are summarized in Table 3.

The data in Table 3 represent behavior of four sets of three samples measured during compressive and tensile tests in air at RT and in liquid nitrogen at 77 K, irrespective of how they were cut from SPS samples.

Table 2. Microhardness HV 0.025 of powder particles and sintered materials

	HV 0.025
Atomized powder	380 ± 20
SPS bulk	370 ± 15

Note the relatively very good reproducibility of all parameters in Table 3 showing stability of the bulk material against variation of the SPS conditions. Substantial is the difference between plasticity of the material in compression and in tension.

3.3 Dislocations in Compression and Fracture in Tension

The transmission electron microscopy (Fig. 6) of the studied bulk material revealed the following. In the as received material there is a very low dislocation density and a network of λ_1 Laves phase particles in B2 matrix grains (Fig. 6a). The material after compressive test at RT displays an inhomogeneous tangle of dislocations (Fig. 6b). Signs of recovery were detected at higher magnifications, i.e. cells with low dislocation density surrounded by cell walls with high density of dislocations with mostly identical Burgers vectors (see Fig. 7). Dislocation tangles contain

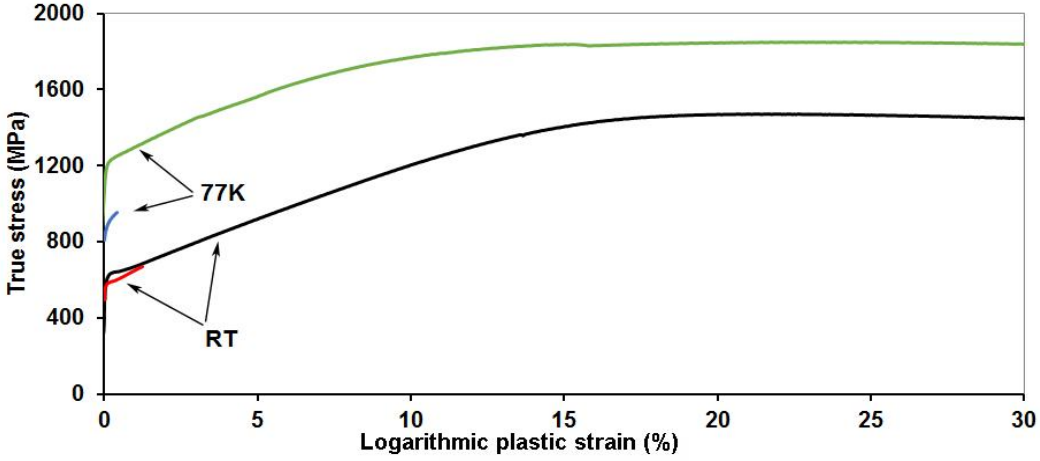

Fig. 5. Compressive (black and green) and tensile (red and blue) true stress vs logarithmic plastic strain curves for the sintered bulk material at RT and 77 K

Table 3. The yield strength σ_{02}, maximum strength σ_{max} and logarithmic plastic strain of the sintered bulk material in air at RT and in liquid nitrogen at 77 K

Temperature	σ_{02} (MPa) (compression, tension)	σ_{max} (MPa) (compression, tension)	Plastic strain (%) (compression, tension)
RT	630 ± 10, 590 ± 10	1530 ± 60, 660 ± 10	> 30, 1.2 ± 0.1
77 K	1215 ± 15, 920 ± 10	1850 ± 10, 950 ± 10	> 30, 0.4 ± 0.1

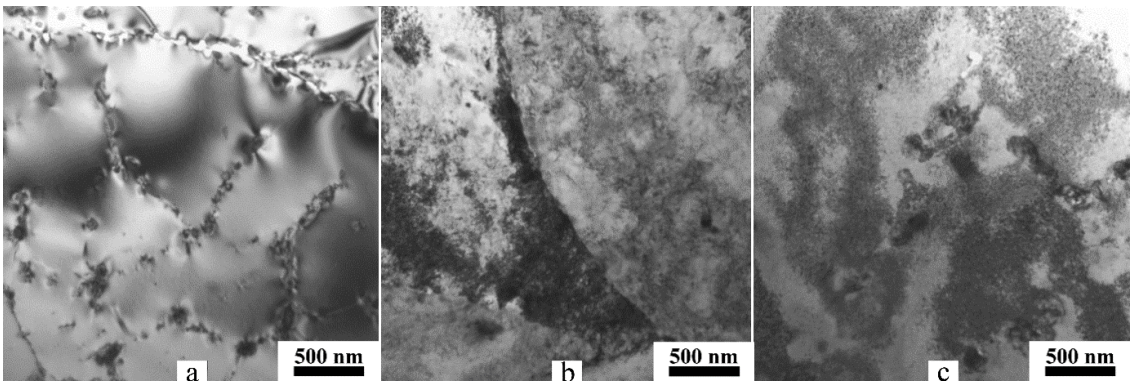

Fig. 6. TEM images of the sintered material: (a) as received; (b) after compressive test at RT; (c) after compressive test at 77 K

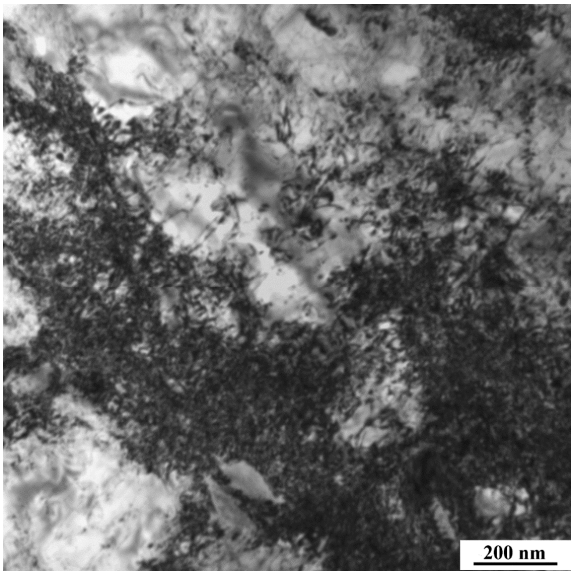

Fig. 7. TEM image of the sintered material after compressive test at RT

dislocations from several different slip systems forming a dense network. The seemingly dislocation-free zone appearing as a gray band on the right side of Fig. 6b is a diffraction contrast artefact that does not show the real dislocation structure of the specimen. However, the material compressed at 77 K contains only high density of homogeneously distributed dislocations with the exception of apparently non-deformed particles (Fig. 6c).

The SEM micrographs of the fracture surface after tensile test show that the fracture occurred in a brittle manner with a nearly planar fracture surface that is perpendicular to the applied tensile stress (Fig. 8). The fracture surface contains evidence of a combination of interparticle and intergranular decohesion and also transgranular cleavage (Fig. 8).

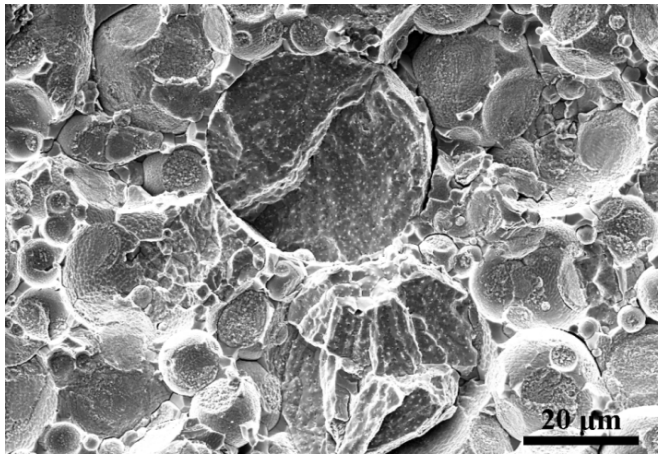

Fig. 8. SEM image of the fracture surface after tensile test at RT

3.4 Elastic Moduli

The density of the bulk material was determined from volume and mass of cuboid-shaped samples and equals to 6290 ± 20 kg.m^{-3}. The density value together with a very good transmission of ultrasonic wave through the samples, confirmed the homogeneity of the SPS material and the absence of macroscopic defects and porosity. Ultrasound velocities were determined by the pulse-echo method in three orthogonal directions. These three velocity values did not mutually differ by more than 1.2 %, therefore the material is isotropic.

The RUS method is based on measurements of the resonant spectrum of free elastic vibrations of the sample, from which the elastic constants are determined via an iterative inverse procedure [12]. The temperature dependence of Young's modulus *E(T)* and shear modulus *G(T)* is shown in Fig. 9. The elastic moduli data for temperatures of performed deformation tests are shown in Table 4.

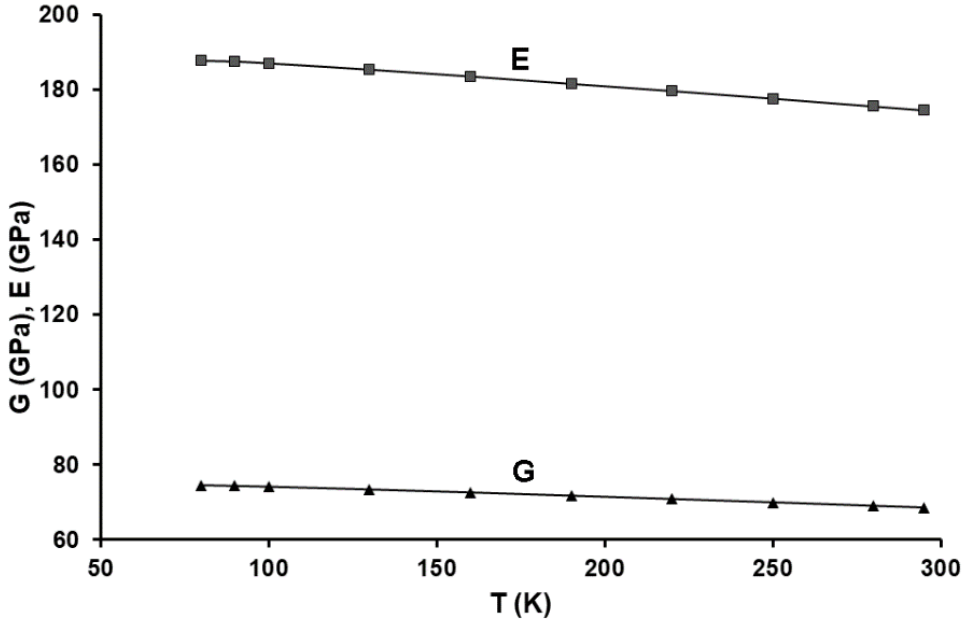

Fig. 9. Temperature dependence of the Young's modulus *E* and shear modulus *G* of the sintered material

Table 4. Elastic moduli *E, G, B* and *B/G* of the sintered material at RT and 80 K.

Temperature	*E* (GPa)	*G* (GPa)	*B* (GPa)	*B/G*
RT	174.4 ± 1.4	68.5 ± 0.3	128 ± 9	1.87 ± 0.12
80 K	187.7 ± 1.4	74.5 ± 0.3	132 ± 9	1.77 ± 0.12

Homogeneous isotropic linear elastic materials have their elastic properties uniquely determined by two moduli. We calculated bulk modulus *B* according to the formula

$$B = \frac{EG}{3(3G - E)}$$

and the ratio *B/G*, introduced by Pugh [16] as a measure of ductility. If *B/G* > 1.75 the material is expected to deform in a plastic manner, whereas the lower values of B/G are associated with brittleness. Values of *B* and *B/G* for temperatures of performed deformation tests are listed in Table 4.

The obtained data do not show any anomaly in the temperature dependence below RT. The Young's modulus at RT for our sintered material is higher or close above the values obtained in [17,18] for binary cast Fe-Al alloy with the same Al – concentration.

3.5 Discussion

The reason for different plasticity of our Fe-Al material in compression and in tension in air can be probably found in the following facts:

1) The environmental embrittlement is often considered as a major cause for the low ductility at RT in air [19]. It is related to high reactivity of Al atoms with the moisture in air. It creates hydrogen that penetrates as atomic hydrogen into material and very probably reduces the surface energy (the strength of interatomic bonds), which lowers the fracture toughness [20,21].

However, it seems that the hydrogen embrittlement phenomenon does not influence the deformation behavior of our material. It may be due to good passivation of the surface of atomized particles that lowers hydrogen diffusivity in the sintered material. No ageing effect or a degradation of the powder has been observed after nearly three years. The improvement of plasticity in compression may be also due to the boron addition that increases grain boundary strength. There may also be an effect of Zr containing λ_1 particles or borides as observed in [2] for a material of nearly the same composition.

2) The poor plasticity in tension is not an intrinsic behavior of the alloy (see dominating role of dislocation motion in compression), but it comes probably from nucleated nano/microcracks between sintered powder particles and/or cavities in originally partly hollow atomized particles. The microcracks open and propagate in the mode I (opening) in tension. Assuming a microcrack nucleates at yielding in tension, the crack propagates immediately after its nucleation when the stress for the crack propagation σ_f is lower than the yield stress σ_y (fracture in a brittle manner). On the other hand, when $\sigma_y < \sigma_f$, the crack propagation could occur only after additional plastic flow giving rise to work hardening, indicating that fracture in tension could be delayed in regions with finer grain size on the basis of the Hall-Petch relationship [22]. The finer grain size regions have higher local yield strength and that may lead to increased ductility of the sintered sample. This effect was observed in polycrystalline isostructural NiAl samples at 673 K [22].

The grain refinement can be achieved by milling of the iron aluminide powder, but this procedure produces also a significant strain hardening of the milled particles. Their microhardness increases according to our measurements typically by about 60% and this strain hardening also leads to the increase of the yield strength of the sintered compact material. However, the milling procedure destroys the passivated surface of atomized particles and then the environmental embrittlement of sintered material can be expected. It is therefore expected that a bulk material prepared from milled powder will have higher strength. On the other hand, such material will be probably also brittle not only in tension, but also in compression.

In case of our measurements in compression the propagation of nucleated or pre-existing nano/microcracks does not occur, the internal stress does not reach a critical value σ_f for a fracture in a brittle manner. The sample in compression has the capacity for plastic deformation and even for the plastic flow (see Fig. 5). After compression, the deformed sample has a typical barrel-shaped form.

3) The influence of temperature below RT on this behavior does not seem to be significant. The observed signs of dynamic recovery at RT only confirm the role of dislocations in compressive deformation. The measured shear modulus values scale with the resistance of the material to plastic deformation and relate this way to its hardness. The relative increase of the yield stress (in both tension and compression) due to the lowering of temperature is naturally higher than the relative increase of the shear modulus value. It is interesting that the corresponding absolute increase of the maximum flow stress σ_{max} in compression is the same as the increase of σ_{02} (and also σ_{max}) in tension. Pugh's values in Table 4 seem to be in agreement with observed plasticity in compression, but the application of this criterion to intermetallic compounds is probably less reliable than for pure metals.

4) Different slip directions in isostructural B2 alloys, the dislocation mobility, and related ductility/brittleness are in general a complex problem [23]. It was generally shown that an interplay of elastic anisotropy of these cubic materials, displacement vectors of metastable planar faults and their energies govern the choice of the activated slip directions [23,24].

4. CONCLUSION

Very good plasticity of the sintered FeAl-based material at both room temperature and 77 K has been evidenced by EBSD of the cryo-milled powder and in compression tests of the sintered material. The TEM observations confirm that dislocations enable the plastic flow in compression at low temperatures. The poor ductility in tension is not an intrinsic behavior of the alloy, but it results from the nucleation and opening of nano/microcracks between sintered powder particles and/or cavities in partly hollow atomized particles.

ACKNOWLEDGEMENTS

This research was supported by the Czech Science Foundation, projects No. 15-15609S and 17-13573S.

COMPETING INTERESTS

Authors have declared that no competing interests exist.

REFERENCES

1. Gaydosh DJ, Draper SL, Nathal MV. Microstructure and tensile properties of Fe-40 at. pct. Al alloys with C, Zr, Hf, and B additions. Metall Trans A. 1989;20A:1701-1713.
2. Morris DG, Morris-Muñoz MA. The influence of microstructure on the ductility of iron aluminides. Intermetallics. 1999;7:1121-1129.
3. Morris DG, Morris-Muñoz MA, Chao J. Development of high strength, high ductility and high creep resistant iron aluminide. Intermetallics. 2004;12:821-826.
4. Baker I. An overview of the mechanical properties of FeAl. Mater Res Soc Symp Proc. 2009;1128:1128-U02-01.
5. Zamanzade M, Barnoush A, Motz C. A review on the properties of iron aluminide intermetallics. Crystals. 2016;6:10. Available:http://dx.doi.org/10.3390/cryst6010010
6. Orrù R, Licheri R, Locci AM, Cincotti A, Cao G. Consolidation/synthesis of materials by electric current activated/assisted sintering. Mater Sci Eng R. 2009;63:127-287.
7. Ji G, Bernard F, Launois S, Grosdidier T. Processing conditions, microstructure and mechanical properties of hetero-nanostructured ODS FeAl alloys produced by spark plasma sintering. Mater Sci Eng A. 2013;559:566-573.
8. Šíma V, Minárik P, Chráska T. Spark plasma sintering of ball milled and atomized powder based on Fe-Al. METAL 2015 – 24th International Conference on Metallurgy and Materials, Conference Proceedings. TANGER Ltd: 2015;1340-1345.
9. Šíma V, Cieslar M, Çelikyürek I, Torun O, Chráska T. Fully dense fine grained FeAl-based intermetallics prepared by spark plasma sintering method. In: Marquis F, editor. Proceedings of the 8th Pacific Rim International Congress on Advanced Materials and Processing (PRICM8). Wiley. 2013;361-368.
10. Skiba T, Haušild P, Karlík M, Vanmeensel K, Vleugels J. Mechanical properties of spark plasma sintered FeAl intermetallics. Intermetallics. 2010; 18:1410-1414.
11. Every AG, Sachse W, editors. Dynamic methods for measuring the elastic properties of solids, Handbook of elastic properties of solids, liquids and gases. Volume I. San Diego: Academic Press; 2001.

12. Leisure RG, Willis FA. Resonant ultrasound spectroscopy. J Phys: Condens Matter. 1997;9:6001-6029.
13. Sedlák P, Seiner H, Zídek J, Janovská M, Landa M. Determination of all 21 independent elastic coefficients of generally anisotropic solids by resonant ultrasound spectroscopy: Benchmark examples. Experimental Mechanics. 2014;54:1073-1085.
14. Morris DG, Gutierrez-Urrutia I, Muñoz-Morris MA. The high-temperature creep behavior of an Fe-Al-Zr alloy strengthened by intermetallic precipitates. Scripta Mater. 2007;57:449-452.
15. Stein F, Sauthoff G, Palm M. Phases and phase equilibria in the Fe-Al-Zr system. Z Metallkd. 2004;94:469-485.
16. Pugh SF. Relations between the elastic moduli and the plastic properties of polycrystalline pure metals. Phil Mag. 1954;45:823-843.
17. Köster W, Gödecke T. Physical measurements on iron-aluminium-alloys between 10 at. percent and 50 at. percent Al. 4. The modulus of elasticity of the alloys. Z Metallkde. 1982; 73:111-114.
18. Frutos E, Morris DG, Morris-Muñoz MA. Evaluation of elasic modulus and hardness of Fe-Al base intermetallics by nano-indentation techniques. Intermetallics. 2013;38:1-3.
19. Liu CT, Lee EH, McKamey CG. An environmental effect as the major cause for room-temperature embrittlement in FeAl. Scr Met. 1989;23:875-880.
20. Zamanzade M, Vehoff H, Barnoush A. Cr effect on hydrogen embrittlement of iron aluminides. Acta Mater. 2014;64:210-223.
21. Yoo MH, Fu CL. Cleavage fracture of ordered intermetallic alloys. Mater Sci Eng A. 1992;153:470-478.
22. Schulson EM, Barker DR. A brittle to ductile transition in NiAl of a critical grain size. Scr Met. 1983;17:519-522.
23. Lin Yi-Shen, Cak M, Paidar V, Vitek V. Why is the slip direction different in different B2 alloys? Acta Mater. 2012;60:881-888.
24. Cao GH, Becker AT, Wu D, Chumbley LS, Lograsso TA, Russel AM, et al. Mechanical properties and determination of slip systems of the B2 YZn intermetallic compound. Acta Mater. 2010;58:4298-4304.

Peer-review history:
The peer review history for this paper can be accessed here:
http://www.sciencedomain.org/review-history/24893